

UC Berkeley

UC Berkeley Previously Published Works

Title

Robust flexural performance and fracture behavior of TiO₂ decorated densified bamboo as sustainable structural materials

Permalink

<https://escholarship.org/uc/item/1gw8p17s>

Journal

Nature Communications, 14(1)

ISSN

2041-1723

Authors

Ba, Ziyu

Luo, Hongyun

Guan, Juan

et al.

Publication Date

2023

DOI

10.1038/s41467-023-36939-6

Copyright Information

This work is made available under the terms of a Creative Commons Attribution License, available at <https://creativecommons.org/licenses/by/4.0/>

Peer reviewed

Robust flexural performance and fracture behavior of TiO₂ decorated densified bamboo as sustainable structural materials

Received: 18 April 2022

Accepted: 24 February 2023

Published online: 04 March 2023

 Check for updates

Ziyu Ba¹, Hongyun Luo^{1,2,3}  , Juan Guan^{1,2}, Jun Luo¹, Jiajia Gao¹, Sujun Wu¹ & Robert O. Ritchie⁴  


High-performance, fast-growing natural materials with sustainable and functional features currently arouse significant attention. Here, facile processing, involving delignification, in situ hydrothermal synthesis of TiO₂ and pressure densification, is employed to transform natural bamboo into a high-performance structural material. The resulting TiO₂-decorated densified bamboo exhibits high flexural strength and elastic stiffness, with both properties more than double that of natural bamboo. Real-time acoustic emission reveals the key role of the TiO₂ nanoparticles in enhancing the flexural properties. The introduction of nanoscale TiO₂ is found to markedly increase the degree of oxidation and the formation of hydrogen bonds in bamboo materials, leading to extensive interfacial failure between the microfibrils, a microfibrillation process that results in substantial energy consumption and high fracture resistance. This work furthers the strategy of the synthetic reinforcement of fast-growing natural materials, which could lead to the expanded applications of sustainable materials for high-performance structural applications.

Biomass composites from animals and plants are increasingly being utilized for the sustainable development of society¹ due to their renewability, high production, and often good mechanical properties^{2,3}. For example, cellulose-based materials can be chemically extracted from materials, such as wood⁴, bamboo^{5,6}, ramie plant⁷ and cotton⁸, with a high surface area and unique morphology; these natural materials display a low density and can achieve a high mechanical strength⁹, which gives them a variety of useful functionalities. Indeed, we see a rapid expansion of wood/cellulose-based nanotechnology¹⁰. To date, the “top-down” approach¹¹ to manufacture high-performance cellulose materials includes delignification of wood or chemical treatment to partially remove lignin and hemicellulose to acquire bulk cellulose scaffolds^{12,13},

densification through hot pressing^{14,15}, vacuum impregnation of resin¹⁶ or mineral substances^{17,18}, freeze-drying¹⁹, carbonization^{20,21}. The impregnation of nanoparticles in wood has usually been enacted for functionalities such as fire retardance¹⁷, magnetic properties¹⁸, and transparency²², whereas the resulting mechanical performance has rarely been examined. Furthermore, most reports on the addition of nanoparticles have focused on the processing of wood, which as a xylophyta grows much slower than herbage such as bamboo.

Constituted by parenchymal cells and vascular bundles, bamboo is a fast-growing natural composite material with a high strength-to-weight ratio and unique natural hierarchical structure^{5,23}. Highly oriented cellulose fibrils in bamboo cells provide stiffness, whereas the

¹School of Materials Science and Engineering, Beihang University, Beijing, P. R. China. ²Beijing Advanced Innovation Centre for Biomedical Engineering, Beihang University, Beijing, P. R. China. ³Beijing Key Laboratory of Advanced Nuclear Materials and Physics, Beihang University, Beijing, P. R. China.

⁴Department of Materials Science & Engineering, University of California, Berkeley, CA 94720, USA.  e-mail: luo7128@163.com; roritchie@lbl.gov

hemicellulose cell walls form the interfaces^{24,25}. However, the uneven distribution of fibers, which can lead to the asymmetric flexural behavior of bamboo, can limit its future application²⁶. Recently, Li et al.²⁷ demonstrated that delignified bamboo could be fabricated into a tough structural material with a uniform fiber distribution by hot pressing; using this technique, the tensile strength of bamboo can be raised to ~1 GPa with a flexural strength as high as 553 MPa. Since the deformation and fracture mechanisms, and hence the resulting toughness, of such modified natural bamboo have never been investigated, the intent of the current work is to examine these aspects in order to seek a deeper understanding of the mechanical performance of densified bamboo.

TiO₂ is a non-hazardous compound with excellent properties for photocatalysis, antifungal use, self-cleaning and hydrogen production, which has been a popular nano-reinforcement in composites^{28–30}. Hydrothermal reactions permit the synthesis of TiO₂ in substrates of wood, bamboo, and cottons with high porosity and water-swelling behavior³¹. In turn, when introducing TiO₂ into bamboo, the photocatalytic activity of the TiO₂ nanoparticles can contribute to the effective antimicrobial property of the bamboo. In addition, the hydroxyl groups on the surface of delignified bamboo provide synthesis sites for TiO₂³². Although a number of studies have sought to investigate the possibility of reinforcing giant reed with graphene oxide (GO) and SiC³³, the in situ synthesis of nanoparticles, such as TiO₂, in bamboo with its mechanical variations have rarely been mentioned. In the current study, a strategy for nanoparticle-reinforced delignified and densified bamboo was developed to induce a series of reinforcement mechanisms to markedly enhance properties.

One remarkable feature of natural bamboo is the high anisotropy of its morphology and fracture behavior; in particular, the toughness of natural bamboo can reach ten times of that of a fibrous composite with the same fraction of fibers³⁴. Various damage mechanisms, especially fiber pull-out, contribute to this high toughness. Such processes can be readily identified by their resulting acoustic signals, which can be assessed using acoustic emission (AE) measurement. Indeed, the technique of AE has been extensively applied for real-time detection of fracture in many metals and composites by analyzing the amplitude, peak frequency, rise time and counts^{35,36}. Previous research suggests that the AE signals during the deformation of bamboo can be associated with the characteristic damage modes, i.e. the fiber fractures generate high-frequency signals, whereas the fracture of the parenchymal cell/matrix generates low-frequency signals^{37,38}. It was therefore reasoned that AE could aid the identification of the salient damage and fracture mechanisms in nanoparticle-reinforced densified bamboo.

Here, we show the fabrication of a composite bamboo by introducing nano-sized TiO₂ particles using a facile hydrothermal synthesis into delignified and densified bamboo. Following characterization of the morphology and chemical properties, we conduct real-time fracture analysis using AE to reveal the various deformation modes and dominant toughening mechanisms in densified and micro-reinforced bamboo. By characterizing the multiple modes of fracture, our objective is to provide guidelines for the design and processing of reinforced natural bamboo materials to inspire their wider application as structural materials.

Results

Morphology and physio-chemical properties of TiO₂-reinforced densified bamboo

Bamboo is a multiscale microstructure fibrous composite; its cross-sectional structure is demonstrated in Fig. 1a. The vascular bundles are embedded in parenchyma cells, consist of microfiber bundles which aggregated microfibers which dimensions of ~15–20 μm. Cuboid bamboo specimens were prepared with the longest side along the direction of the growth of mature bamboo. The three-step processing involved the removal of lignin and hemicellulose by boiling in NaOH and Na₂SO₃ solutions, vacuum impregnation and hydrothermal

synthesis of TiO₂ in a reaction bath, and then densification by hot pressing (Fig. 1b and Supplementary Fig. 1). With such processing, the density of the bamboo material was increased by ~91% from 0.7 to 1.34 g/cm³ (Fig. 1c). After the alkali treatment, the peaks at 1423 cm⁻¹ and 1510 cm⁻¹ in the Fourier transform infrared (FTIR) spectra (characteristic of stretching vibrations of the benzene ring in lignin) and the peaks at 1850–1600 cm⁻¹ (characteristic of stretching vibrations of the carboxyl group in xylan in hemicellulose) were decreased (Fig. 1d); this indicates the removal of lignin and hemicellulose from the bamboo^{39,40}. Such chemical delignification caused the oxygen/carbon (O/C) ratio to increase from 0.23 to 0.60 (Table 1). X-ray diffraction (XRD) analysis also showed that all the characteristic peaks for the crystalline phase of cellulose-I, (101), (002) and (040), were present in the TiO₂-modified densified bamboo. The enlarged XRD peaks at 2θ = 25.3°, 37.8°, and 48.0° (Fig. 1g), corresponding to the (101), (004), and (200) planes of anatase TiO₂ (JCPDS 21-1272), served to confirm the successful synthesis of the TiO₂. In addition, from the scanning electron microscopy (SEM) in Fig. 1e, f and Supplementary Fig. 2 and X-ray photoelectron spectroscopy (XPS) in Fig. 1h, the TiO₂ particles can be seen to have been successfully introduced into the bamboo.

The detailed morphologies of natural, densified and TiO₂-modified bamboo are compared in Fig. 2a–h. In natural bamboo, parenchymal cells with numerous micrometer- and nanometer-sized voids together with bamboo microfiber bundles (aggregation of microfibers between vascular bundles) can be seen to be aligned adjacent to each other (Fig. 2a, b), the voids allowing the easy vacuum impregnation of fluids or reaction solutions. The delignification process removed most of the lignin and hemicellulose in the bamboo. As shown in the computed micro-tomography in Supplementary Fig. 3, ~190-μm-sized voids were generated between the vessels when the parenchyma cells were broken after the alkali treatment. Such voids can be compressed easily to produce denser bamboo materials using hot pressing. Compared to natural bamboo, the parenchyma cells are highly compact in the densified bamboo (Fig. 2c, d and Supplementary Fig. 3). The bamboo microfibers (single fiber of vascular bundles with dimensions of ~15–20 μm) become slightly twisted following the hot alkali treatment, but still remain highly aligned at the macroscale. This causes the 2D small-angle X-ray scattering (SAXS) patterns, shown in Fig. 2n and Supplementary Fig. 4, to transition from a rhombus shape in natural bamboo into a spindle shape after the treatment. These scattering patterns indicate the unchanged orientation of parallel cellulose fibers in the equator direction after the removal of lignin and hemicellulose and after the densification, similar to that reported in ref.⁴¹.

Figure 2e shows that both the cell walls and vascular fibers of natural bamboo become decorated with TiO₂ particles after the hydrothermal reaction; some aggregates of TiO₂ particles, with dimensions ~500 nm to 1 μm, also appear at the interfaces of fibers of TiO₂-densified bamboo, as shown in Fig. 2g, h and Supplementary Fig. 5. The thickness of the TiO₂-densified bamboo was ~1.2–1.5 mm (Supplementary Fig. 6), with TiO₂ nanoparticles detected at ~0.5 mm beneath the surface but not in the middle regions, probably because the reaction solution was not able to infiltrate completely into the internal bamboo cell walls. In addition, the bamboo matrix was also seen to form cracks due to the swelling stresses resulting from the high temperature of 120 °C in hot-pressing process.

To further reveal the differences in the chemical composition, peak deconvolution analysis was performed on the C and O peaks of the high-resolution XPS spectrum of natural and TiO₂-modified bamboo (Fig. 2i–l). The C 1s peak of the XPS spectra was mainly deconvoluted into three peaks (C1, C2, and C3) and the O 1s peak into two peaks^{42,43} (O1 and O2), with each peak associated with a different chemical bond (as detailed in Table 1). After delignification and densification, the C1 peak decreased from 84 to 57% and O1 decreased from 40 to 19%, which is related to the removal of hydrocarbons, i.e., lignin–phenylpropane and wax. The C2 peak, which corresponds to

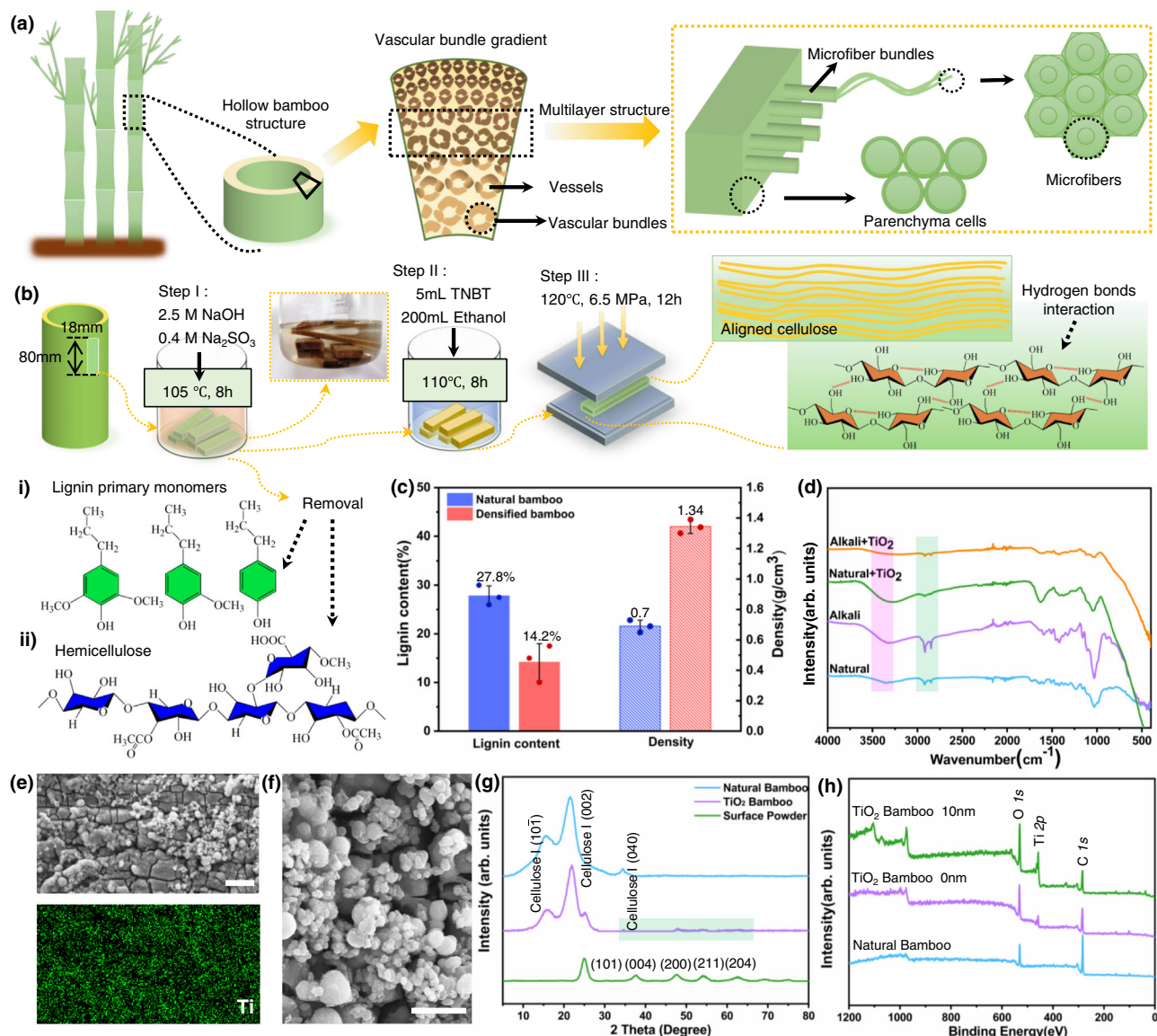


Fig. 1 | The preparation and characterization of densified TiO₂ bamboo.

a Multilevel structure of bamboo. **b** The three-step processes including delignification, synthesis of TiO₂ and hot pressing. TNBT is the abbreviation of tetrabutyl titanate. **(i)** Lignin primary monomers, **(ii)** hemicellulose. **c** Lignin content and density of natural bamboo and densified bamboo. Data are presented as mean values ± SEM, n = 3 independent samples. **d** FTIR spectra of natural, alkali-treated and TiO₂ decorated bamboo. The highlighted region, pink: the hydrogen groups,

green: the methyl groups. **e** SEM and Energy-dispersive spectroscopy (EDS) images of TiO₂ distribution on inner natural bamboo, inset EDS with color green: titanium. Scale bar is 10 μm. **f** High-magnification of SEM image, scale bar is 5 μm. **g** XRD patterns of natural bamboo, TiO₂-decorated bamboo. The highlighted region in green: TiO₂ on bamboo. **h** XPS spectra of natural bamboo and TiO₂-decorated bamboo.

C–OH/C–O–C mainly from cellulose in bamboo, increased significantly from 14% to 40%. The area of C2 and C3 peaks together signify the presence of oxygenated carbon C_{ox}; the area of C1 peak signifies the presence of unoxygenated carbon C_{unox}. Accordingly, the ratio of C_{ox}/C_{unox} can be calculated from the following Eq. (1)⁴²:

$$C_{ox}/C_{unox} = \frac{C2 + C3}{C1}, \quad (1)$$

The C_{ox}/C_{unox} ratio of the bamboo materials in Table 1 increased from 0.19 to 0.75 during the delignification process, further indicative of significant oxidation and removal of lignin and hemicellulose (Supplementary Fig. 7 and Tables 1 and 2). Moreover, the 25.3% increase in the C2 peak (C–OH/CO–C) is an indication of more hydrogen bond interactions⁴⁴, which is likely to be advantageous for mechanical performance. The elemental O/C ratio in delignified

bamboo, shown in Table 1, was found to be close to that of cellulose⁴⁴. The Ti 2p peaks in Fig. 1h in fact possess two characteristic peaks of Ti 2p_{1/2} at 464.6 eV and Ti 2p_{3/2} at 458.9 eV in Fig. 2m. The binding energy difference of 5.7 eV between the Ti 2p_{1/2} peak and Ti 2p_{3/2} peak reveals a valence state of +4 for Ti, indicating that Ti was in the form of TiO₂ in the samples²⁸.

Taken together, the TiO₂-reinforced densified bamboo was seen to be successfully prepared from natural bamboo, with the anisotropic morphology of cellulose fibers being maintained despite the change in chemical composition.

Flexural mechanical performance of TiO₂-reinforced densified bamboo

The flexural mechanical properties of natural bamboo, densified bamboo, and TiO₂-reinforced densified bamboo are compared in Fig. 3 and Table 2. The direction of the bending load was the same as the gradient

Table 1 | Atomic composition (%) and peak deconvolution results of the C 1s peak (the corresponding bonds) obtained by XPS analysis

	C	O	Ti	O/C	C1 (C-C, C-H)	C2 (C-O-C/C-OH)	C3 (O-C-O/C=O)	C _{ox} /C _{unox}
Natural	81.27%	18.73%	0	0.23	83.75%	14.43%	1.82%	0.19
TiO ₂ -Reinforced	60.3%	35.91%	3.79%	0.60	57.23%	39.73%	3.04%	0.75

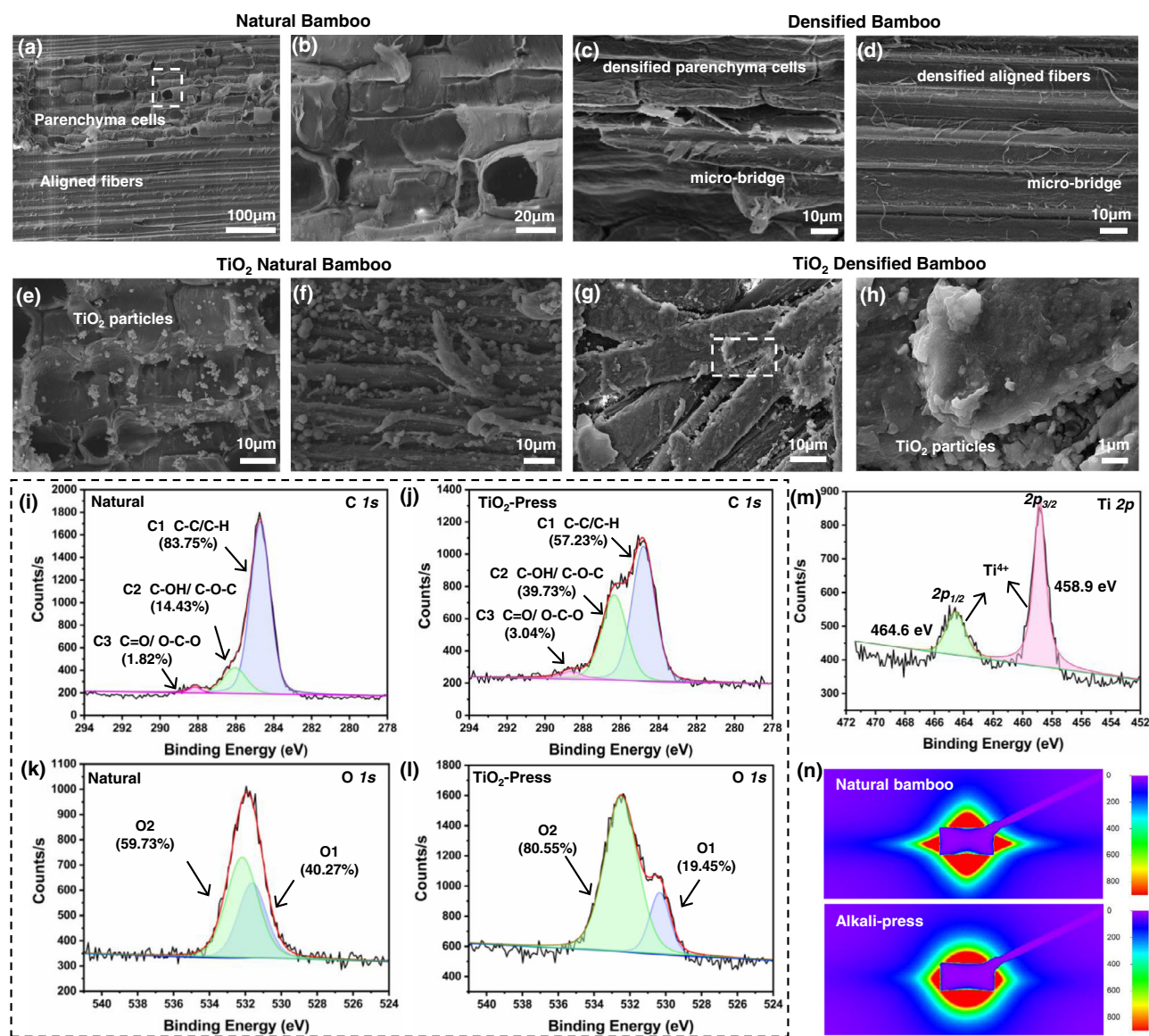


Fig. 2 | Morphology and chemical group composition of the bamboo materials. SEM images of (a, b) natural bamboo, white dashed line in (a) shows the SEM magnification region of (b). c Densified parenchyma cells in densified bamboo. d Densified aligned fibers. e, f TiO₂-decorated bamboo, TiO₂ particles on (e) parenchyma cells and (f) bamboo fibers. g, h TiO₂ densified bamboo, white dashed line in (g) shows the SEM magnification region of (h). i, j High-resolution XPS spectra of

C 1s peaks at 282–290 eV of (i) natural bamboo, j densified TiO₂ bamboo. k, l High-resolution XPS spectra of O 1s peaks of (k) natural bamboo, (l) densified TiO₂ bamboo. m High-resolution XPS spectra of Ti 2p peaks of densified TiO₂-decorated bamboo. n Small-angle X-ray scattering (SAXS) patterns of natural bamboo and densified bamboo.

of the fiber density in bamboo. As shown in Fig. 3b, c, alkali-treated densified bamboo showed a flexural strength of 333 MPa, whereas the TiO₂-reinforced densified bamboo demonstrated the highest flexural strength of 418 MPa, i.e., over 190% larger than that of natural bamboo. The flexural strength of 333 MPa for densified bamboo was similar to that reported in ref. ²⁷; after decoration with the TiO₂ nanoparticles, the flexural strength became higher than the reported 404 MPa for similar densified outer bamboo. Thus, the reinforcement effect of TiO₂ nanoparticles was clearly significant. The flexural strength of the

bamboo material was improved by 26% after TiO₂ reinforcement, with the flexural modulus increasing from 21 GPa to 31 GPa; additionally, a higher specific flexural strength of 311 MPa cm³ g⁻¹ was also seen (Supplementary Fig. 8). Moreover, after TiO₂ reinforcement, the tensile strength increased to 392 MPa, i.e., a ~22% improvement (Supplementary Fig. 9). Given that the mass increase from the introduction of TiO₂ particles was minimal, the effect of reinforcement with 3.8% Ti atoms on the mechanical properties of bamboo can be considered to be particularly significant (Table 1).

Table 2 | Flexural properties of different bamboo specimens

Materials	Stress [MPa]	Modulus [GPa]	Breaking energy [MJ m^{-3}]
Natural	124.5 ± 17.67	10.25 ± 1.63	7.66 ± 1.16
Alkali-Press	332.59 ± 15.39	20.78 ± 2.9	20.08 ± 1.98
TiO ₂ -Reinforced	417.91 ± 36.68	31.12 ± 3.79	26.12 ± 3.56

The side view of various bamboo materials based on SEM imaging is shown in Fig. 3e–j. It can be seen that the crack path of the densified bamboo was serrated, exhibiting a small deflection angle along the vertical direction under bending (Fig. 3e). Specifically, the hot-pressing procedure compressed the microfibril bundles and parenchyma cells to result in a “sandwich-type” morphology. Nonetheless, cracks tended to propagate along the interface between the cells and fibers leading to delamination (laminar debonding), although crack bridging by the parenchyma cells was also evident (Fig. 3f). However, the overall fracture morphology of the TiO₂-reinforced densified bamboo was much rougher. A clear fracture feature was the fibrillation of microfibril

bundles with the pull-out of multiple bamboo microfibrils along with the interfacial delamination of the parenchyma cells (Fig. 3h–j). The vertical crack path in the TiO₂-reinforced densified bamboo was largely deflected causing the separation of the fibers and the cells (Fig. 3h). The majority of fibers could be seen to be bridging the cracks, which is a potent extrinsic toughening mechanism³⁴ that further consumes energy during the fracture of TiO₂-densified bamboo. For densified bamboo, the delamination of cells and the fracture of microfibril bundles were the two dominant damage modes. In contrast, fibrillation and the fracture of individual fibers were the two dominant damage modes of the TiO₂-densified bamboo. Supplementary Fig. 10 and 11 also evidence the strengthening enhancement of TiO₂-densified bamboo; however, it should be noted that although the TiO₂ nanoparticles were difficult to detect in the middle of the specimens, the occurrence of fibrillation and single fibers buckling still showed a significant influence of TiO₂ decoration on the bamboo material.

Figure 4 shows the morphology of flexural fracture of the bottom and top planes. For the bottom plane with the largest flexural strain, the densified bamboo fracture showed a serrated crack with

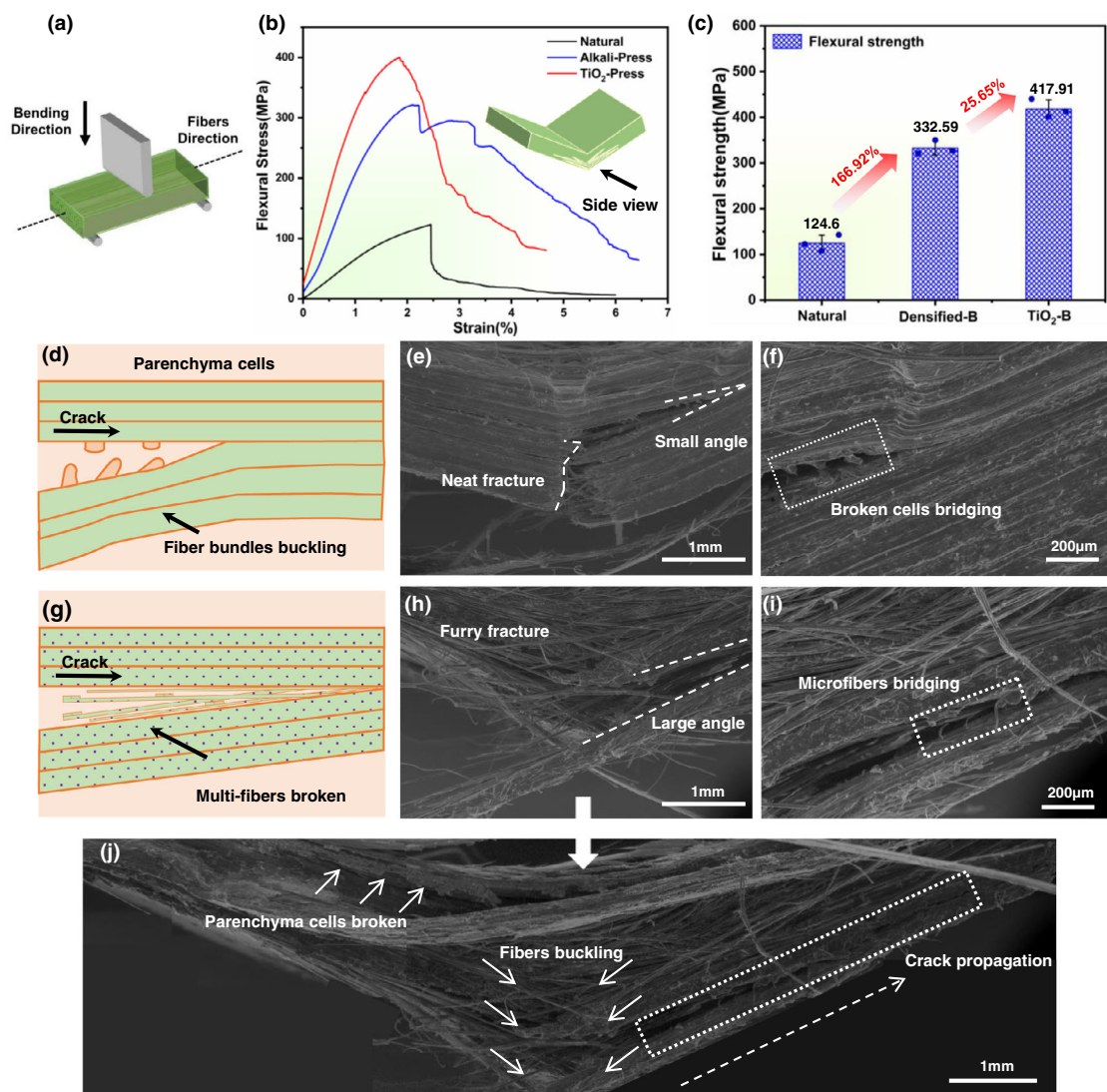


Fig. 3 | Flexural properties and SEM of the morphology fracture of bamboo. **a** Schematic diagram of the flexural test. **b** Flexural stress-strain curves of natural, densified and TiO₂-densified bamboo. **c** The improvement of natural, densified and TiO₂-densified bamboo. Data are presented as mean values ± SEM, $n = 3$ independent samples. **d** Schematic diagram of the morphology of the fracture of densified

bamboo. **e, f** SEM image of the fracture of densified bamboo, **(e)** neat fracture, **(f)** broken cells bridging. **g** Schematic diagram of the fracture morphology of TiO₂-densified bamboo. **h–j** SEM image of the fracture of TiO₂-densified bamboo, the furry fracture of **(h)**, **(i)**, and the full fracture image in **(j)**.

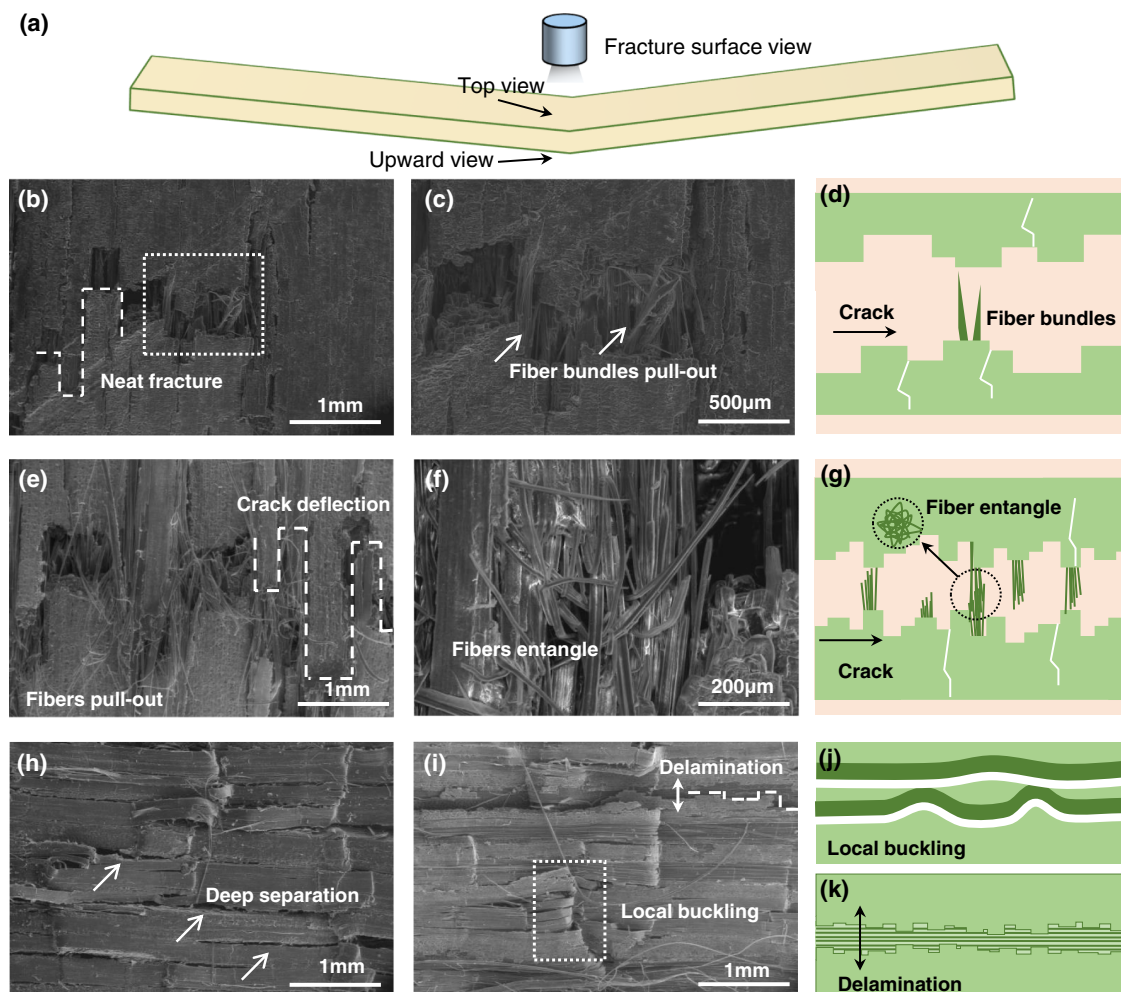


Fig. 4 | SEM morphology fracture of top and upward view of densified and TiO₂-densified bamboo. **a** Schematic of the observation view. **b, c** Upward view of densified bamboo fracture, (**b**) neat fracture, and the magnification image in (**c**). **d** Schematic diagram of morphology upward view fracture of densified bamboo. **e, f** Upward view of TiO₂-densified bamboo fracture, (**e**) microfibrils pulled out, (**f**)

fibers entangle. **g** Schematic diagram of morphology upward view fracture of TiO₂-densified bamboo. **h** Top view SEM morphology of densified bamboo. **i** Top view SEM morphology of TiO₂-densified bamboo. **j, k** Schematic diagram of top view fracture behavior of bamboo, (**j**) local buckling, (**k**) delamination.

the pull-out of microfiber bundles (Fig. 4b, c), whereas the fracture of the TiO₂-reinforced densified bamboo involved a critical fracture mechanism of fibrillation⁴⁵, which refers to the dissociation of microfibrils within the fibers. After fibrillation, the bamboo microfibrils were further pulled out with some creating bridges across the serrated crack (Fig. 4e). It is readily apparent that the presence of the TiO₂ nanoparticles promotes the fibrillation of the microfiber bundles in densified bamboo, which is an important mechanism to enhance the toughness and damage-tolerance of bamboo⁴⁶. Indeed, Fig. 4h, i shows that deep cracks appeared on the top surface of both bamboo materials, indicating delamination and buckling of the fibers and parenchyma cells. Such a buckled or wavy crack morphology can increase the bending stiffness, and the deflection of cracks can further provide extrinsic toughening⁴⁷.

To summarize, the SEM fractography of the bamboo materials revealed that the introduction of 3.8% TiO₂ nanoparticles resulted in a fracture mode transition. The fracture mode changed from cracking with the pull-out of microfiber bundles to cracking associated with fibrillation and pull-out of bamboo microfibrils. The latter mechanisms resulted in a marked increase in the strength and toughness of the bamboo due to the presence of the TiO₂ reinforcement, quantitatively to a respective improvement in both flexural strength and modulus by -26% and -50% (Table 2).

Real-time flexural fracture process analysis by acoustic emission

As noted above, acoustic emission (AE) is a widely used non-destructive analytical tool to monitor the fracture process as well as to distinguish different fracture modes of structural materials (such as matrix fracture, delamination, fiber fracture, etc.)^{38,48}. As shown in Fig. 5, AE was employed to monitor the flexural fracture process of two bamboo materials. The AE peak frequency signals can be generally associated with matrix fracture, delamination, and fiber fracture of bamboo at various low to high frequencies. The characteristic AE peak frequency signals of the microfiber bundle fracture and fiber separation / delamination were first identified by stretching a bamboo microfiber bundle (diameter ~90 µm) (Fig. 5c). The corresponding AE signals were concentrated at frequency bands of ~100 kHz for fiber separation / delamination and ~200 kHz for microfiber bundle fracture according to earlier studies^{37,38}. Figure 5d-f shows typical AE signals from natural, densified and TiO₂-reinforced densified bamboo materials during flexural deformation. Due to the unique gradient structure of natural bamboo, a large number of matrix fracture signals were generated and usually concentrated in the frequency band 130–160 kHz⁴⁹ (termed Types I to III). In addition, a large number of 220–250 kHz (Type IV) high-frequency signals was also generated for the densified bamboo (Fig. 5e), which were

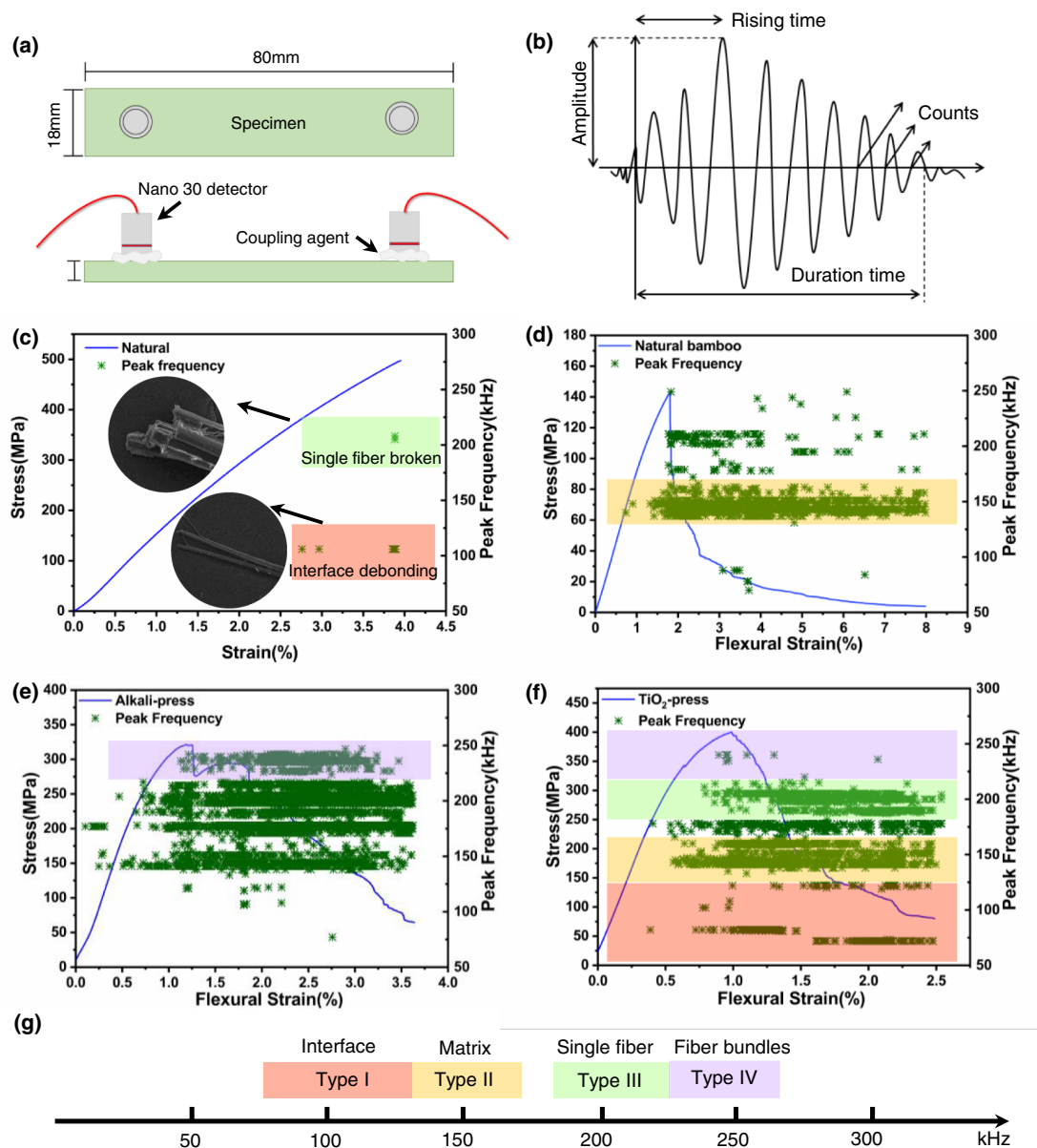


Fig. 5 | Representative damage modes and real-time acoustic emission (AE) peak frequency signals in natural, densified, and TiO₂-densified bamboo.

a Schematic diagram of AE set-up. **b** AE signal characteristics. **c** AE signals of tensile fracture of single bamboo fiber with the identified Type I and Type III signals in red and green highlight. **d** AE signals of natural bamboo flexural process with the

identified Type II signals in yellow highlight. **e** AE signals of densified bamboo flexural process with the identified Type IV signals in purple. **f** AE signals of TiO₂-densified bamboo flexural process with classification of four types of signals.

g Classification of AE signals. To clarify the signal classification, all types of signals are only highlighted in (f).

attributed to microfibril bundle fracture. The frequency signals can thus be classified in terms of 50–130 kHz (Type I), 130–160 kHz (Type II), 180–220 kHz (Type III), and 220–250 kHz (Type IV) in Fig. 5g.

It was clear that the number of Type I acoustic signals from the TiO₂-reinforced densified bamboo was much higher (Fig. 5f) than that from densified bamboo (Fig. 5e) due to the significantly increased fibrillation and delamination between fibers and TiO₂-reinforced parenchyma cells (Figs. 3j and 4e); additionally, there was increased friction between the rougher crack surfaces in the TiO₂-reinforced material (Supplementary Fig. 12). Notably, Type IV signals were significantly less frequent than Type III signals, suggesting that single fiber fracture was more prominent than microfibril bundle fracture.

To understand the acoustic spectra, the amplitude of the AE peaks can be associated with the energy to create the damage. For the

various bamboo materials subjected to flexural deformation, the AE amplitude was analyzed to indicate four types of damage modes in Fig. 6. The lower amplitude signals from TiO₂-densified bamboo indicated more microscale damage with a lower AE energy (shown in Supplementary Fig. 13). This can be related to the fibrillation and friction between fibers and densified parenchyma cells of TiO₂-densified bamboo. After the maximum flexural stress, ~90% of AE signals were detected. Type II signals characteristic of the matrix cracking were generated, principally in natural bamboo (Fig. 6a), followed by a small number of Type IV signals characteristic of microfibril bundle fracture⁵⁰. In contrast, the densified bamboo generated approximately six times more numerous Type III and Type IV signals than natural bamboo (Fig. 6b). Type I, Type II and Type III signals were dominant for the TiO₂-reinforced densified bamboo. In particular, Type I signals appeared at the early stage of flexural deformation of the TiO₂-reinforced densified bamboo, indicating that fibrillation was occurring

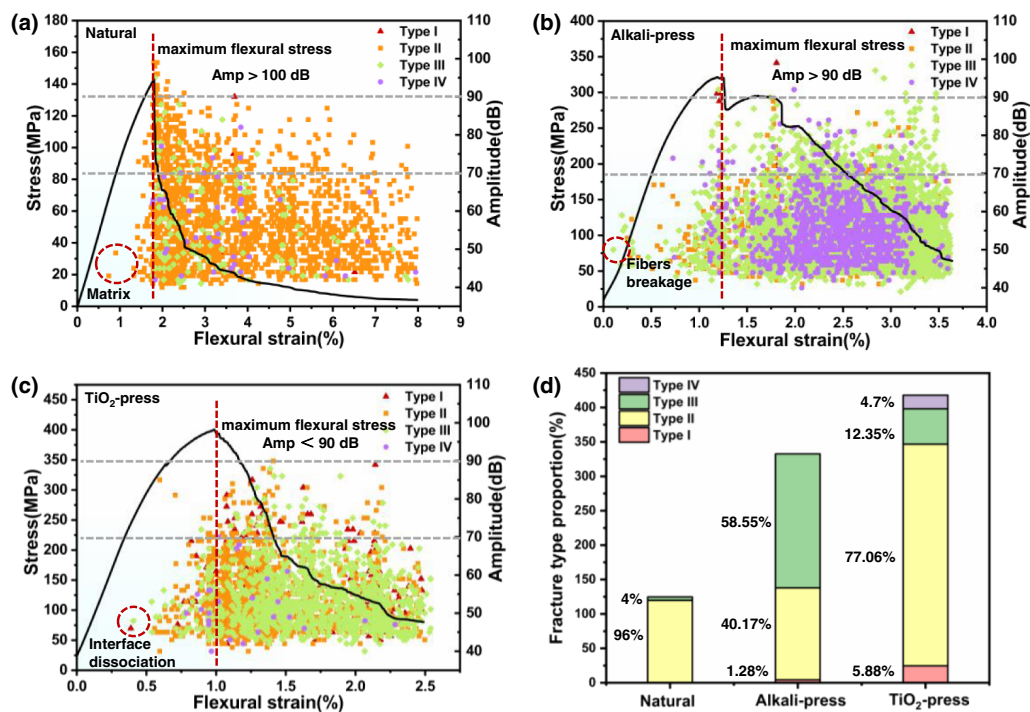


Fig. 6 | Signal distribution (amplitude and peak frequency) during the flexural deformation of natural, densified, and TiO₂-densified bamboo. a Natural bamboo. **b** Densified bamboo. **c** TiO₂-densified bamboo. The gray dashed line in (a–c) divides the amplitude of AE signals into three parts: 30–70, 70–90, and 90–110 dB,

respectively. **d** Proportion of different AE signals representing different fracture mechanisms in the three bamboo materials prior to the point of maximum flexural stress (Red dashed line in a–c).

prior to the fiber pull-out and fracture (Fig. 6c). Clearly as shown in Fig. 6d and Table 3, the number of AE signals associated to various damage modes and energies prior to the maximum flexural stress was quite distinct for the three bamboo materials. Matrix cracking, through densified parenchyma cells, was the most prominent (~96%) in natural bamboo, with matrix fracture and fiber fracture prominent in the densified bamboo. The introduction of TiO₂ definitively suppressed the fracture of microfiber bundles, from ~59 to 12%, transitioning to single fiber fracture and fiber dissociation/fibrillation. It should be noted that the combination of fracture modes induced in the TiO₂-reinforced densified bamboo is completely consistent with its more than threefold higher fracture energy compared to natural bamboo. TiO₂-reinforced densified bamboo definitely displays enhanced toughness.

Toughening mechanisms in TiO₂-reinforced densified bamboo

As natural fiber composite materials, bamboo materials with a fiber-and-parenchyma cell matrix morphology showed extensive delamination/fibrillation, fiber pull-out, microfiber bridging prior to outright fracture. We revealed, using SEM imaging and acoustic emission (AE), that the dominant strengthening and toughening mechanisms during the flexural deformation can vary significantly depending on whether TiO₂ particles were introduced into the bamboo material. For the TiO₂-reinforced densified bamboo, fibrillation of the microfiber bundle and

microfiber fracture were most prominent, which resulted in enhanced flexural toughness. Additional toughening was likely achieved through the friction between the bamboo microfibrils. Due to these fracture processes, the crack path under flexural loading became significantly tortuous, being deflected within the “fiber-parenchyma cells-fiber” structure of TiO₂-reinforced densified bamboo, a scenario that further served to increase the toughness of this material. It is noted that these fracture events in TiO₂-reinforced densified bamboo are active at micrometer length scales, which primarily affect the extrinsic toughness of bamboo materials.

Figure 7 illustrates these fracture events to indicate the specific micro-effects of the TiO₂ particles in TiO₂-reinforced densified bamboo. In this material, although the bamboo was compressed and chemically strengthened by the introduction of hydroxyl groups and extensive hydrogen bonding, the interfaces among parenchyma cells remained weakly bonded, leading to cell delamination and microfiber bundle separation and eventually microfiber bundle fracture (Fig. 7a). However, the TiO₂ particles distributed in the cells and fibers not only exerted a bridging effect between the fibers and matrix, but also rendered the separation of fibers/fibrillation in the microfiber bundles to be more prevalent (as shown in Fig. 7a, b). The angle of the cracks within the fibers also tended to decrease after the addition of TiO₂ nanoparticles⁵¹, which may further act to toughen the composite bamboo material by increasing crack deflection and energy dissipation. It is apparent that the fibrillation process in the TiO₂-reinforced bamboo provides a potent contribution to the flexural toughness of this material.

Table 3 | Number of Type I–IV AE signals and different amplitude of AE signals prior to the maximum flexural stress

Samples	Peak frequency				Amplitude		
	Type I	Type II	Type III	Type IV	35–70	70–90	>90
Natural	0	72	3	0	46	25	0
Alkali-Press	3	94	137	0	318	21	4
TiO ₂ -Press	10	131	21	8	233	9	0

Discussion

A three-step processing procedure was applied to transform natural bamboo into a high-flexural-performance bamboo composite. The first step of delignification removed most of the lignin and hemicellulose, introduced a large number of hydroxyl groups, and preserved the cellular morphology and highly oriented fibrous

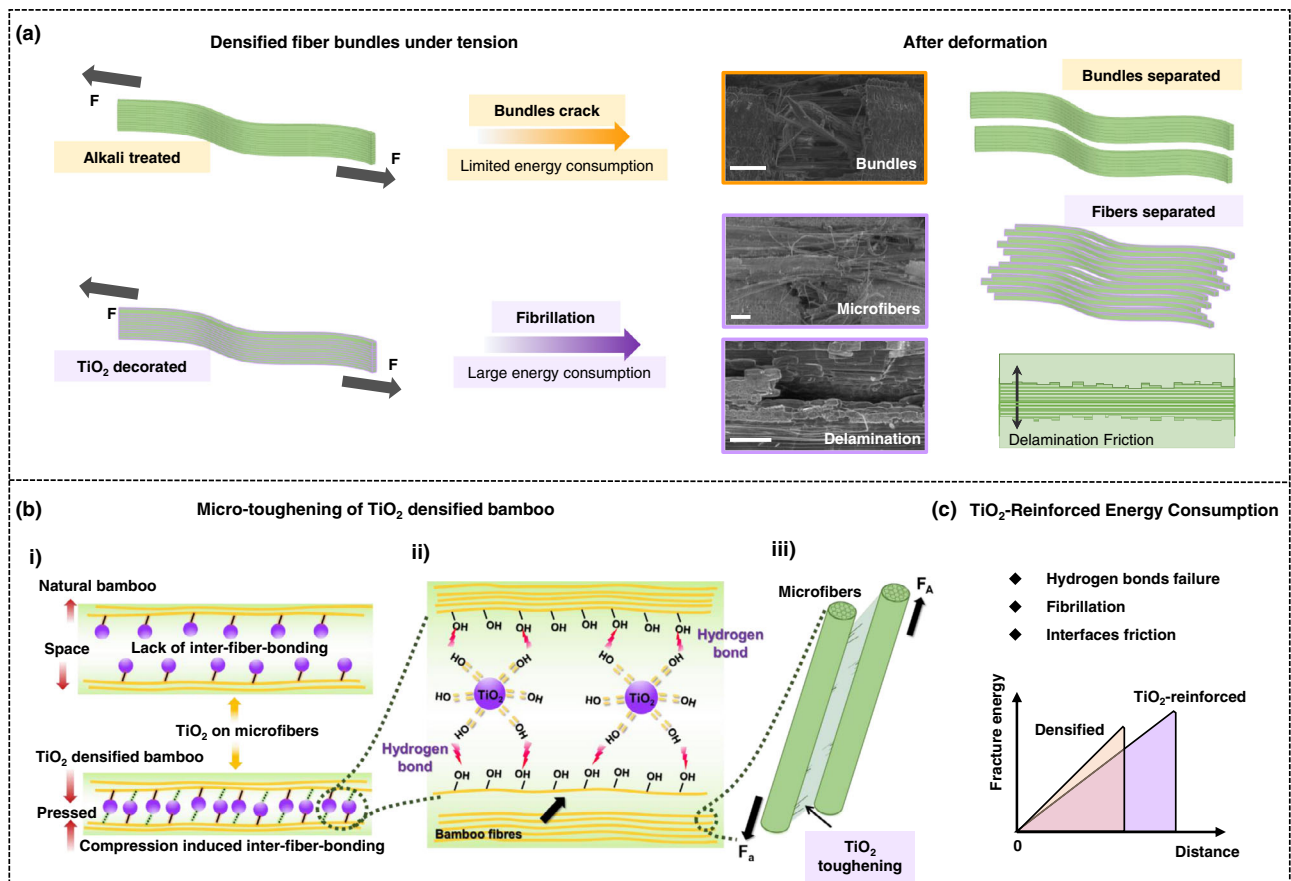


Fig. 7 | Schematic diagram of the salient mechanisms of how TiO₂ reinforcements can improve the flexural property of densified bamboo. a Deformation to fracture of densified and TiO₂-reinforced densified bamboo under tension. Scale bars: 200 μ m. **b** Micro TiO₂-reinforcement mechanisms in the flexural deformation

process. (i) Bonding mode of TiO₂ on natural and densified bamboo. (ii) Hydrogen bonds of TiO₂-reinforced densified bamboo. (iii) TiO₂ toughening between bamboo microfibers. **c** Energy consumption of TiO₂-reinforced densified bamboo.

structure of bamboo. The second step of hydrothermal synthesis successfully introduced TiO₂ nanoparticles in the cells and on the fibers of the bamboo. The final step compressed the material to a compact fiber composite. Such processing led to a significantly elevated flexural strength of 418 MPa for the TiO₂-reinforced densified bamboo, i.e., three times of that of natural bamboo. We attribute these outstanding flexural properties not only to the introduction of hydrogen bonds between aligned fibers and TiO₂ nanoparticles but also to microfiber separation, both of which promote energy dissipation during fracture. This study provides a strategy of in situ synthesis of TiO₂ particles reinforcement for natural porous materials as well as a facile way to identify fracture mechanisms in natural and modified structural materials. The reinforcement of TiO₂ establishes an efficient means to significantly improve the flexural mechanical performance of natural bamboo, which should expand the structural applications of this promising natural resource.

Methods

Materials and chemicals

Moso bamboos were purchased from the Hunan province of China and were processed into cuboid specimens with two sets of sizes, 80 × 18 × 6 mm for natural bamboo, and 80 × 18 × 1.5 mm for densified bamboo. Specimens were cut at -1.5 m from the bottom of 5-year-old mature bamboo. NaOH (AR, Beijing chemical reagent company) and Na₂SO₃ (AR, Beijing chemical reagent company) were used in the delignification process to remove lignin and hemicellulose. C₂H₆O (AR, Beijing Chemical Reagent Company) and tetrabutyl titanate ($\geq 99.0\%$, Aladdin) were used to synthesize the TiO₂.

Preparation of TiO₂-decorated bamboo

To explore the effect of synthesis conditions on TiO₂ nanoparticle formation, tetrabutyl titanate (TNBT) with varied concentrations, 0.015 M, 0.025 M, and 0.035 M, was dissolved in ethanol absolute, respectively, and the solutions stirred for 30 min; the bamboo was then submerged in the solution under a low vacuum (0.1 bar) for 2 h. Subsequently, the bamboo specimens that were impregnated with the TNBT solution were put into a reaction bath at 110 °C for 4 h. After ultrasonic cleaning in ethanol absolute and deionized water for multiple times, the specimens were dried in an oven at 60 °C for further SEM and flexural mechanical tests (Supplementary Figs. 14 and 15). Owing to its appropriate particle size and distribution, 0.025 M TNBT was chosen as the solution for the investigation of the role of TiO₂ nanoparticle reinforcements in influencing the flexural fracture behavior of densified bamboo.

Preparation of densified-TiO₂ bamboo

The bamboo specimens were manufactured into densified TiO₂ bamboo using three steps. In the first step, bamboo specimens were boiled in 2.5 M NaOH and 0.4 M Na₂SO₃ for 8 h, then the specimens were washed in water several times to remove residual alkali until the pH reached -7. Then 5 mL tetrabutyl titanate was dissolved in 200 mL of absolute ethyl alcohol and the solution stirred for 30 mins; the delignified bamboo was then submerged in the solution under a low vacuum (0.1 bar) for 2 h. Subsequently, the delignified bamboo specimens that were impregnated with solution were put into a reaction bath at 110 °C for 4 h. The processed specimens were pressed at 120 °C under a compressive stress of 6.5 MPa for 12 h to

generate the delignified, TiO₂-reinforced and densified bamboo. The raw bamboo without any treatment, delignified bamboo followed by hot pressing, and TiO₂-decorated densified bamboo were termed as “natural bamboo”, “densified bamboo” and “TiO₂-densified bamboo”, respectively. The lignin content (Klason lignin) of these bamboo materials was measured according to the TAPPI method (TAPPI T 222 om-02)⁵²: Specifically, 3 mL 72 wt.% H₂SO₄ was added into 0.2 g (*M*) bamboo powder and reacted for 1 h. The H₂SO₄ solution was then diluted to 3 wt.% and the mixture heated in an oven at 120 °C ± 3 °C for 1 h. After the solution was cooled down and filtered, the residual was dried at 105 °C ± 3 °C until the mass (*m*) was stable. The content of lignin was calculated according to Eq. (2):

$$\text{Content of lignin} = \frac{m}{M} \times 100\% \quad (2)$$

The density of our bamboo specimens was measured as follows. All the specimens were dried in an air-flow oven at 80 °C ± 3 °C until the mass of the specimens was stable. The specimens were then placed under the same ambient conditions (20–25 °C, 30–40% relative humidity) to reach the same hydration state, prior to the mass *M* being measured. The volume of the specimens did not change during such ambient conditioning; their size also did not change after the treatment. Cuboid specimens with the above-mentioned sizes, corresponding to volumes of *V* = 8640 mm³ for natural bamboo and *V* = 2160 mm³ for densified bamboo. The density was calculated from *M/V*, based on measurements on three specimens; mean values are presented.

Mechanical testing

The tensile and flexural tests of bamboo specimens were conducted on a mechanical testing machine (SANS, MTS Industrial System Co. Ltd., China) operating at a displacement rate of 1 mm/min under ambient conditions. The dimensions of these specimens were 80 × 18 × 6 mm for natural bamboo and 80 × 18 × 1.5 mm for densified and decorated densified bamboo, respectively; all samples were unnotched. Strain-stress curves were generated using origin software (originlab 9.0), and illustrations were finalized using Power Point 2013 software.

Microstructure and morphology analysis

Fourier transform infrared (FTIR) spectroscopy of the specimens was determined using a Nicolet Magna IR560, spectrometer, with the spectral range from 4000 to 400 cm⁻¹. A field-emission scanning electron microscope (FESEM, ZEISS ULTRA 55, Germany) with an accelerating voltage of 10 kV and a low vacuum mode was used to characterize the morphologies of natural and densified-TiO₂ bamboo using the secondary electron mode. The chemical characterization of Ti was analyzed in an energy-dispersive spectrometer (EDS) equipped with the FESEM. Computed micro-tomography was performed at beamline 4W1A at the Beijing Synchrotron Radiation Facility (BSRF, Beijing, China) with an X-ray energy of 15 keV. Fracture morphologies were observed using an optical microscope (OM, Leica DM400, Leica Microsystems, Germany). The modified, as well as the unmodified, bamboo was analyzed using X-ray diffraction (XRD, Rigaku Corp., Tokyo, Japan) by Jade software v6.2. X-ray photoelectron spectroscopy (XPS) was measured (ULVAC-PHI Quantera SXM, INC) at a pass energy of 0.1 eV with Al Kα as the X-ray source, and the data was analyzed by XPSpeak software v4.1. Small-angle X-ray scattering (SAXS) was performed at 1W2A beamline of the Beijing Synchrotron Radiation Facility using a beam size of 1 × 0.4 mm², with the 2D scattering patterns collected from the data processing software Fit2D (v18.002).

Acoustic emission

The acoustic emission (AE) technique was applied to detect the acoustic signals during flexural mechanical test arising from damage and cracking events. All the signals were collected by two piezoelectric sensors (Nano-30, frequency of 140 kHz with band-pass filtering of 150–400 kHz), and were analyzed using a digital signal processor with an AEwin v3.61 AE system (Physical Acoustic Corporation, USA). To improve the conduction of the signals between the specimens and detectors, Vaseline was smeared on the surface of sensors. To filter the noise acoustic signals from other environmental sources, an amplitude acquisition threshold of 40 dB was used in all experiments.

Reporting summary

Further information on research design is available in the Nature Portfolio Reporting Summary linked to this article.

Data availability

The data that support the findings of this study are available within this paper or included in the Supplementary Information. Source data are provided with this paper.

References

- Jiang, F. et al. Wood-based nanotechnologies toward sustainability. *Adv. Mater.* **30**, 1703453 (2018).
- Yang, K. et al. Integrating tough *Antheraea pernyi* silk and strong carbon fibres for impact-critical structural composites. *Nat. Commun.* **10**, 3786 (2019).
- Yang, K., Yazawa, K., Tsuchiya, K., Numata, K. & Guan, J. Molecular interactions and toughening mechanisms in silk fibroin-epoxy resin blend films. *Biomacromolecules* **20**, 2295–2304 (2019).
- Gan, W. et al. Single-digit-micrometer thickness wood speaker. *Nat. Commun.* **10**, 5084 (2019).
- Salvati, E. et al. Multiscale analysis of bamboo deformation mechanisms following NaOH treatment using X-ray and correlative microscopy. *Acta Biomater.* **72**, 329–341 (2018).
- Li, Z. et al. Sustainable high-strength macrofibres extracted from natural bamboo. *Nat. Sustain.* **5**, 235–244 (2021).
- Yang, X. & Berglund, L. A. Water-based approach to high-strength all-cellulose material with optical transparency. *ACS Sustain. Chem. Eng.* **6**, 501–510 (2017).
- Ye, D. et al. Ultrahigh tough, super clear, and highly anisotropic nanofiber-structured regenerated cellulose films. *ACS Nano* **13**, 4843–4853 (2019).
- Habibi, Y., Lucia, L. A. & Rojas, O. J. Cellulose nanocrystals: chemistry, self-assembly, and applications. *Chem. Rev.* **110**, 3479–3500 (2010).
- Berglund, L. A. & Burgert, I. Bioinspired wood nanotechnology for functional materials. *Adv. Mater.* **30**, e1704285 (2018).
- Song, J. et al. Processing bulk natural wood into a high-performance structural material. *Nature* **554**, 224–228 (2018).
- Jia, C. et al. From wood to textiles: top-down assembly of aligned cellulose nanofibers. *Adv. Mater.* **30**, e1801347 (2018).
- Frey, M. et al. Delignified and densified cellulose bulk materials with excellent tensile properties for sustainable engineering. *ACS Appl. Mater. Interfaces* **10**, 5030–5037 (2018).
- Wei, J. et al. Laminating wood fiber mats into a densified material with high performance. *Mater. Lett.* **253**, 358–361 (2019).
- Medina, L. et al. Nanostructure and properties of nacre-inspired clay/cellulose nanocomposites—synchrotron X-ray scattering analysis. *Macromolecules* **52**, 3131–3140 (2019).
- Li, Y., Fu, Q., Yu, S., Yan, M. & Berglund, L. Optically transparent wood from a nanoporous cellulose template: combining functional and structural performance. *Biomacromolecules* **17**, 1358–1364 (2016).

17. Fu, Q. et al. Nanostructured wood hybrids for fire-retardancy prepared by clay impregnation into the cell wall. *ACS Appl. Mater. Interfaces* **9**, 36154–36163 (2017).
18. Merk, V., Chanana, M., Gierlinger, N., Hirt, A. M. & Burgert, I. Hybrid wood materials with magnetic anisotropy dictated by the hierarchical cell structure. *ACS Appl. Mater. Interfaces* **6**, 9760–9767 (2014).
19. Wan, J. et al. Highly anisotropic conductors. *Adv. Mater.* **29**, 1703331 (2017).
20. Li, T. et al. Scalable and highly efficient mesoporous wood-based solar steam generation device: localized heat, rapid water transport. *Adv. Funct. Mater.* **28**, 1707134 (2018).
21. Chen, C. et al. Scalable and sustainable approach toward highly compressible, anisotropic, lamellar carbon sponge. *Chem* **4**, 544–554 (2018).
22. Zhu, M. et al. Highly anisotropic, highly transparent wood composites. *Adv. Mater.* **28**, 5181–5187 (2016).
23. Youssefian, S. & Rahbar, N. Molecular origin of strength and stiffness in bamboo fibrils. *Sci. Rep.* **5**, 11116 (2015).
24. Liu, Z. et al. Adaptive structural reorientation: developing extraordinary mechanical properties by constrained flexibility in natural materials. *Acta Biomater.* **86**, 96–108 (2019).
25. Chen, C. et al. Rapid processing of whole bamboo with exposed, aligned nanofibrils toward a high-performance structural material. *ACS Nano* **14**, 5194–5202 (2020).
26. Habibi, M. K., Samaei, A. T., Gheshlaghi, B., Lu, J. & Lu, Y. Asymmetric flexural behavior from bamboo's functionally graded hierarchical structure: underlying mechanisms. *Acta Biomater.* **16**, 178–186 (2015).
27. Li, Z. et al. A strong, tough, and scalable structural material from fast-growing bamboo. *Adv. Mater.* **32**, e1906308 (2020).
28. Li, J. et al. Visible-light-mediated antifungal bamboo based on Fe-doped TiO₂ thin films. *RSC Adv.* **7**, 55131–55140 (2017).
29. Li, J. et al. Growth of TiO₂ coating on wood surface using controlled hydrothermal method at low temperatures. *Appl. Surf. Sci.* **256**, 5046–5050 (2010).
30. Sun, Q. et al. Hydrothermal fabrication of rutile TiO₂ submicrospheres on wood surface: an efficient method to prepare UV-protective wood. *Mater. Chem. Phys.* **133**, 253–258 (2012).
31. Zhao, Y. et al. Frost-resistant high-performance wood via synergistic building of omni-surface hydrophobicity. *Chem. Eng. J.* **385**, 123860 (2020).
32. Li, J. et al. Fabrication of superhydrophobic bamboo timber based on an anatase TiO₂ film for acid rain protection and flame retardancy. *RSC Adv.* **5**, 62265–62272 (2015).
33. Novel, D. et al. Strengthening of wood-like materials via densification and nanoparticle intercalation. *Nanomaterials* **10**, 478 (2020).
34. Launey, M. E. & Ritchie, R. O. On the fracture toughness of advanced materials. *Adv. Mater.* **21**, 2103–2110 (2009).
35. Li, Y., Ma, H., Shen, Y., Li, Q. & Zheng, Z. Effects of resin inside fiber lumen on the mechanical properties of sisal fiber reinforced composites. *Compos. Sci. Technol.* **108**, 32–40 (2015).
36. Groot, P. J. D., Wijnen, P. A. M. & Janssen, R. B. F. Real-time frequency determination of acoustic emission for different fracture mechanisms in carbon/epoxy composites. *Compos. Sci. Technol.* **55**, 405–412 (1995).
37. Chen, G. et al. Flexural deformation and fracture behaviors of bamboo with gradient hierarchical fibrous structure and water content. *Compos. Sci. Technol.* **157**, 126–133 (2018).
38. Chen, G., Luo, H., Yang, H., Zhang, T. & Li, S. Water effects on the deformation and fracture behaviors of the multi-scaled cellular fibrous bamboo. *Acta Biomater.* **65**, 203–215 (2018).
39. Cabane, E., Keplinger, T., Kunniger, T., Merk, V. & Burgert, I. Functional lignocellulosic materials prepared by ATRP from a wood scaffold. *Sci. Rep.* **6**, 31287 (2016).
40. Xu, G., Wang, L., Liu, J. & Wu, J. FTIR and XPS analysis of the changes in bamboo chemical structure decayed by white-rot and brown-rot fungi. *Appl. Surf. Sci.* **280**, 799–805 (2013).
41. Crawshaw, J., Bras, W., Mant, G. R. & Cameron, R. E. Simultaneous SAXS and WAXS investigations of changes in native cellulose fiber microstructure on swelling in aqueous sodium hydroxide. *J. Appl. Polym. Sci.* **83**, 1209–1218 (2002).
42. Popescu, C.-M., Tibirna, C.-M. & Vasile, C. XPS characterization of naturally aged wood. *Appl. Surf. Sci.* **256**, 1355–1360 (2009).
43. Meng, F.-D., Yu, Y.-L., Zhang, Y.-M., Yu, W.-J. & Gao, J.-M. Surface chemical composition analysis of heat-treated bamboo. *Appl. Surf. Sci.* **371**, 383–390 (2016).
44. Jie, C. *Cellulose Science and Materials* (Chemical Industry Press, 2015).
45. Al-Turaif, H. A. Effect of nano TiO₂ particle size on mechanical properties of cured epoxy resin. *Prog. Org. Coat.* **69**, 241–246 (2010).
46. Wang, L. et al. Review on nonconventional fibrillation methods of producing cellulose nanofibrils and their applications. *Biomacromolecules* **22**, 4037–4059 (2021).
47. Ahmad, F., Yuvaraj, N. & Bajpai, P. K. Influence of reinforcement architecture on static and dynamic mechanical properties of flax/epoxy composites for structural applications. *Composite Struct.* **255**, 112955 (2021).
48. Tian, W. et al. Impact of hydration on the mechanical properties and damage mechanisms of natural silk fibre reinforced composites. *Compos. Part A: Appl. Sci. Manuf.* **147**, 106458 (2021).
49. Ramirez-Jimenez, C. R. et al. Identification of failure modes in glass/polypropylene composites by means of the primary frequency content of the acoustic emission event. *Compos. Sci. Technol.* **64**, 1819–1827 (2004).
50. Monti, A., El Mahi, A., Jendli, Z. & Guillaumat, L. Mechanical behaviour and damage mechanisms analysis of a flax-fibre reinforced composite by acoustic emission. *Compos. Part A: Appl. Sci. Manuf.* **90**, 100–110 (2016).
51. Faber, K. T. Crack deflection processes. I. *Theory Acta Met.* **31**, 565 (1983).
52. Technical Association of the Pulp and Paper Industry (TAPPI). Acid-insoluble lignin in wood and pulp. *T222 Om-02*, 1–7 (2011).

Acknowledgements

The authors wish to thank the staff of the Beijing Synchrotron Radiation Facility beamline (1W2A) and Shanghai Synchrotron Radiation Facility beamline (BL19U2) for the help with the SAXS experiments. This work was supported by the National Key Research, Development Program of China (No. 2017YFF0210002), and the program of the Ministry of Industry and Information Technology of China (J2019-VI-0001-0114) to H.Y.L. ROR was supported by the Multi-University Research Initiative grant #AFOSR-FA9550-15-1-0009 from the Air Force Office of Scientific Research specifically through a subcontract to the University of California Berkeley.

Author contributions

J.J.G. and H.Y.L. designed the experiments. J.J.G. and Z.Y.B. carried out the mechanical tests and characterization tests. Z.Y.B., J.L., and H.Y.L. collectively analyzed the data and wrote the initial draft of the paper. H.Y.L., J.G., S.W., and R.O.R. were involved in the supervision of the work, discussion of the results and revision of the manuscript. All the authors edited and reviewed the final manuscript.

Competing interests

The authors declare no competing interests.

Additional information

Supplementary information The online version contains supplementary material available at <https://doi.org/10.1038/s41467-023-36939-6>.

Correspondence and requests for materials should be addressed to Hongyun Luo or Robert O. Ritchie.

Peer review information *Nature Communications* thanks the anonymous reviewer(s) for their contribution to the peer review of this work.

Reprints and permissions information is available at <http://www.nature.com/reprints>

Publisher's note Springer Nature remains neutral with regard to jurisdictional claims in published maps and institutional affiliations.

Open Access This article is licensed under a Creative Commons Attribution 4.0 International License, which permits use, sharing, adaptation, distribution and reproduction in any medium or format, as long as you give appropriate credit to the original author(s) and the source, provide a link to the Creative Commons license, and indicate if changes were made. The images or other third party material in this article are included in the article's Creative Commons license, unless indicated otherwise in a credit line to the material. If material is not included in the article's Creative Commons license and your intended use is not permitted by statutory regulation or exceeds the permitted use, you will need to obtain permission directly from the copyright holder. To view a copy of this license, visit <http://creativecommons.org/licenses/by/4.0/>.

© The Author(s) 2023